Faceted spurs at normal fault scarps : Insights from numerical modeling

Carole Petit, Yanni Gunnell, N. Gonga-Saholiariliva, Bertrand Meyer, J. Seguinot

To cite this version:

Carole Petit, Yanni Gunnell, N. Gonga-Saholiariliva, Bertrand Meyer, J. Seguinot. Faceted spurs at normal fault scarps : Insights from numerical modeling. Journal of Geophysical Research : Solid Earth, 2009, 114 (B05403), pp.1-20. ⟨10.1029/2008JB005955⟩. ⟨hal-00421910⟩

HAL Id: hal-00421910
https://hal.science/hal-00421910v1

Submitted on 17 May 2021

JOURNAL OF GEOPHYSICAL RESEARCH, VOL. 114, B05403, doi:10.1029/2008JB005955, 2009

Faceted spurs at normal fault scarps: Insights from numerical modeling

C. Petit,[1] Y. Gunnell,[2] N. Gonga-Saholiariliva,[2] B. Meyer,[1] and J. Séguinot[3]

Received 24 July 2008; revised 7 February 2009; accepted 27 February 2009; published 8 May 2009.

[1] We present a combined surface processes and tectonic model which allows us to determine the climatic and tectonic parameters that control the development of faceted spurs at normal fault scarps. Sensitivity tests to climatic parameter values are performed. For a given precipitation rate, when hillslope diffusion is high and channel bedrock is highly resistant to erosion, the scarp is smooth and undissected. When, instead, the bedrock is easily eroded and diffusion is limited, numerous channels develop and the scarp becomes deeply incised. Between these two end-member states, diffusion and incision compete to produce a range of scarp morphologies, including faceted spurs. The sensitivity tests allow us to determine a dimensionless ratio of erosion, *f*, for which faceted spurs can develop. This study evidences a strong dependence of facet slope angle on throw rate for throw rates between 0.4 and 0.7 mm/a. Facet height is also shown to be a linear function of fault throw rate. Model performance is tested on the Wasatch Fault, Utah, using topographic, geologic, and seismologic data. A Monte Carlo inversion on the topography of a portion of the Weber segment shows that the 5 Ma long development of this scarp has been dominated by a low effective precipitation rate ($\sim$1.1 m/a) and a moderate diffusion coefficient (0.13 m^2/a). Results demonstrate the ability of our model to estimate normal fault throw rates from the height of triangular facets and to retrieve the average long-term diffusion and incision parameters that prevailed during scarp evolution using an accurate 2-D misfit criterion.

Citation: Petit, C., Y. Gunnell, N. Gonga-Saholiariliva, B. Meyer, and J. Séguinot (2009), Faceted spurs at normal fault scarps: Insights from numerical modeling, *J. Geophys. Res.*, *114*, B05403, doi:10.1029/2008JB005955.

1. Introduction

[2] Faceted spurs or triangular facets are geomorphologic features frequently observed at normal fault scarps [e.g., *Cotton*, 1950; *Birot*, 1958]. Whereas spectacular faceted spurs are currently observed in regions of active extension such as the Basin and Range [e.g., *Wallace*, 1978], Baikal Rift [*Houdry*, 1994; *San'kov et al.*, 2000], and Aegean region [e.g., *Armijo et al.*, 1991; *Meyer et al.*, 2002; *Ganas et al.*, 2005], other areas affected by active extension show weakly incised normal fault scarps lacking faceted spurs (Figure 1). In contrast to reverse faulting, which creates a gravitationally unstable topography due to relative uplift of the hanging wall above the ground surface, normal faulting allows topographic expression of fault surfaces to be maintained in the landscape for relatively longer periods of time. Once a topographic step is formed above the hanging wall, the normal fault scarp is progressively incised by drainage [e.g., *Hamblin*, 1976; *Wallace*, 1978]. This process can generate triangular facets in which facet summits correspond to the termination of a topographic spur forming a strike-perpendicular interfluve between V-shaped valleys in the incised footwall. Triangular facets are thus landforms that bear the influence of tectonic (i.e., fault dip, earthquake recurrence intervals, amount of coseismic slip) and external (incision and diffusion rates, landsliding) parameters. For example, the so-called wineglass canyons that flank faceted spurs in many regions are generated by a combination of footwall uplift and increased fluvial incision that has been occurring since the last glacial maximum [e.g., *Wallace*, 1978; *Benedetti et al.*, 1998; *Goldsworthy and Jackson*, 2000]. As shown later, tectonics, fluvial incision and in situ diffusion on hillslopes are governed by specific rules, and different combinations of these have different impacts on the shapes of faceted spurs. As a result, these can be used as quantitative tectonic and climatic markers.

[3] Inferring the tectonic signal from the analysis of topography has long been a challenge to geomorphologists. Some studies have attempted to extract the tectonic signal from the analysis of river long profiles and drainage slope distribution [e.g., *Wobus et al.*, 2006; *Whittaker et al.*, 2007, 2008], based on scaling laws between channel slopes and contributing drainage areas. Alongside these analytic studies, numerical landscape evolution models (LEMs), also called surface process models (SPMs), have proved to be useful tools in predicting topographic evolution relating to tectonic and erosive processes on both small [e.g., *Anderson*,

---

[1] ISTeP, UMR 7193, UPMC, CNRS, Paris, France.

[2] Laboratoire de Géographie Physique, UMR 8591, Université Paris VII, CNRS, Paris, France.

[3] LGIT, Université Joseph Fourier, Grenoble, France.

0148-0227/09/2008JB005955$09.00

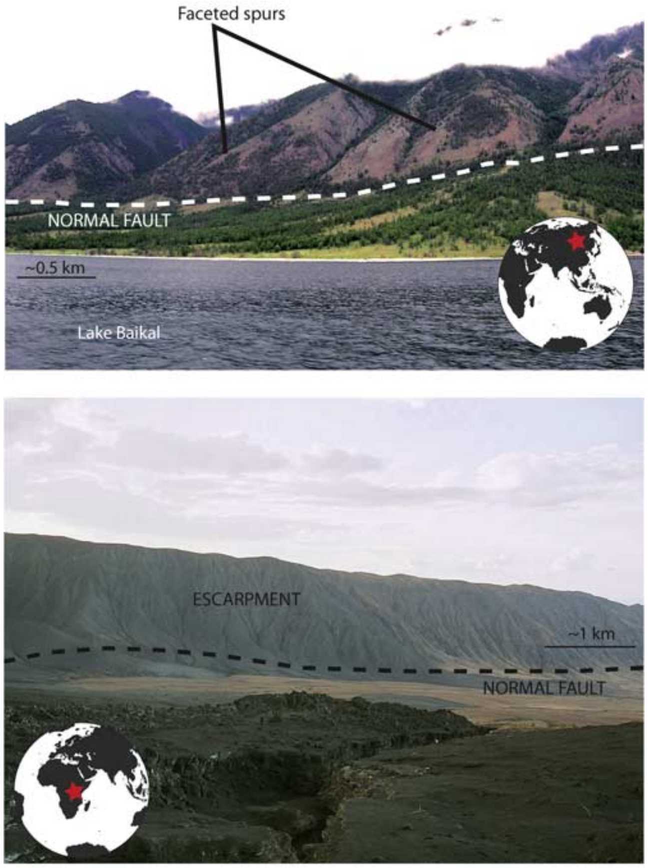

Figure 1. Two examples of active normal fault scarps. (top) Faceted scarp along the western shore of Lake Baikal, Siberia. (bottom) Nonfaceted scarp on the Natron fault system, East African rift, Tanzania.

1994; *Gilchrist et al.*, 1994; *Kooi and Beaumont*, 1994; 1996; *Cowie et al.*, 2006; *Attal et al.*, 2008] and large [e.g., *Densmore et al.*, 1998; *Ellis et al.*, 1999; *Lague et al.*, 2003] spatial and temporal scales [*Merritts and Ellis*, 1994]. Reviews of the algorithms governing landscape evolution are given by *Coulthard* [2001], *Dietrich et al.* [2003], *Codilean et al.* [2006], and *Braun* [2006]. Until now, however, the development of faceted spurs has not been a primary focus of most SPM studies (*Ellis et al.* [1999] excepted). Among other SPM studies focused on extensional tectonics, *Cowie et al.* [2006] modeled the development and evolution of a drainage system during the growth and linkage of normal faults, but the large grid spacing used (~1 km) is not suited to the characterization of faceted spurs which are typically 1–2 km wide. *Allen and Densmore* [2000] studied the evolution of sediment supply from the uplifting footwall in response to tectonic and climatic changes. These and later similar studies [*Densmore et al.*, 2004, 2007] show models that produce faceted spurs, but they do not discuss this precise topic.

[4] *Densmore et al.* [1998] studied the evolution of normal fault-bounded mountains while focusing on the importance of landsliding. Following this study, *Ellis et al.* [1999] modeled the development of the Basin and Range topography using the Zscape algorithm which includes vertical motions along one or several normal faults, and a combination of fluvial incision, linear diffusion and stochastic landsliding. Their model produces triangular facets, which the authors interpret as being predominantly generated by landsliding. According to this study, triangular faceted spur morphology is entirely controlled by rock strength, which defines the maximum slope angle under which the facet remains stable. These authors also concluded that facet height probably bears no relation to fault slip rate. However, several observations have allowed us to question these conclusions. First, triangular facets commonly display a convex topographic profile with steepening slopes at the scarp base of the scarp. This militates in favor of progressive fault plane exhumation and restrained scarp erosion rather than for massive landsliding. Second, as noticed by *Ellis et al.* [1999], the products of such frequent landslides are not observed in the field and some faceted spurs still retain components of the fault plane. Third, the strange-looking topography generated by Zscape when the landsliding function is switched off [*Densmore et al.*, 1998] suggests that mass movement is probably overestimated in the model formulation.

[5] In this paper, we present sensitivity tests performed with a coupled surface processes and tectonic model. The tests allow us to separately determine the climatic and tectonic parameters (fault slip rate, fault dip) that control the development and morphology of faceted spurs. We show that the morphology of triangular facets does retain some information about the tectonic processes. The model is tested against topographic and geologic data from the Wasatch Fault, Utah.

2. Tectonic and Surface Process Model

[6] We developed a SPM that incorporates long-scale fluvial erosion and short-scale diffusion on a regular grid, inspired by previous formulations by *Kooi and Beaumont* [1994] and *Braun and Sambridge* [1997]. The SPM is mixed with a kinematic uplift model which simulates the activity of a normal fault following the elastic dislocation solution of *Okada* [1985]. We tested model sensitivity to climatic parameters over an 8 × 4 km grid with a grid spacing of 0.1 km, and the model was run for 1.5 Ma with a time step of 1 ka. The time duration of the model ensures that the output topography has reached a steady state in which crustal and erosional processes are balanced, and that facet growth is achieved [see, e.g., *Ellis et al.*, 1999].

2.1. Surface Process Model

[7] Hillslope transport is modeled using a linear diffusion law where the rate of erosion is linearly related to the curvature of the topographic slope:

$$\frac{\partial h}{\partial t} = K_D \Delta h \tag{1}$$

where Δ is the Laplace operator, h is the elevation, t is time and K_D is the diffusion coefficient. Different diffusion coefficients can be used for the bedrock and regolith. Mass conservation is verified by the computation of the diffusive flux, q_D:

$$\begin{aligned} \vec{q_D} &= -K_D \cdot \vec{\mathrm{grad}}\,(h) \\ \frac{\partial h}{\partial t} &= \mathrm{div}(q_D) \end{aligned} \tag{2}$$

In this model, the coefficient of diffusion is artificially increased (multiplied by 1.5) when the local slope exceeds a threshold of 40° in order to simulate mass movement conditions such as landsliding. The diffusion equation is solved using an explicit finite difference approximation.

[8] Fluvial erosion is simulated using a uniform effective precipitation rate, v_r, over the entire grid and a linear stream power law in which the equilibrium sediment flux is proportional to river discharge and to local topographic slope:

$$q_{eq} = K_f q_r \frac{\partial h}{\partial l} \tag{3}$$

where q_{eq} is the equilibrium flux, or carrying capacity of the river, i.e., the flux of sediment $[\mathrm{VT}^{-1}]$ that a river can transport for a given slope and catchment area. K_f is a transport coefficient; q_r is the local water discharge (integral of the upstream effective precipitation, v_r) and $\partial h/\partial l$ is local slope in the stream direction. Effective precipitation v_r is total precipitation, P, weighted by a runoff coefficient <1, whereby $v_r < P$. Parameter v_r, therefore, corresponds to the rainfall effectively engaged in runoff and erosion processes, not in vegetation uptake, evaporation, rock weathering, or groundwater recharge. In this way precipitation and hillslope diffusivity can be treated in the SPM as independent variables. Local discharge is computed by integrating the upstream precipitation on the principle that each cell of the model transfers all of its surface water to only one of its eight neighbors in the direction of the maximum slope (D8 method of *O'Callaghan and Mark* [1984]). The discharge is computed iteratively for each grid point by decreasing order of altitude. The rate of incision depends on the imbalance between carrying capacity, q_{eq}, and the local sediment flux, q_f, generated by erosion upstream:

$$\frac{\partial h}{\partial t} = (q_f - q_{eq})/wL_f \tag{4}$$

where w is the channel width (assumed constant) and L_f is a characteristic transport length that depends on the detachability of channel bed materials [e.g., *Beaumont et al.*, 1992; *Kooi and Beaumont*, 1994]. According to Beaumont et al. and Kooi and Beaumont, L_f is a characteristic length scale of the river long profile and corresponds to the distance along the channel where erosion changes from detachment-limited conditions to transport-limited conditions. L_f can vary spatially to simulate different detachability thresholds of the substratum. If net sediment flux exceeds carrying capacity, L_f decreases to allow rapid deposition of excess sediments. The assumption of a constant w is justified here by the observation that channel widths in footwall uplands tend to be constant upstream of the active boundary fault [*Whittaker et al.*, 2007]. The assumption of uniform precipitation rate is consistent with the relatively small catchment areas (<10 km^2) defined within the model grid surface. Incision due to debris flows in the upper part of the catchments [e.g., *Stock and Dietrich*, 2003] is neglected. Surface runoff, fluvial incision or deposition and diffusive fluxes are computed at each time step. Water and sediments are allowed to flow out of the model grid space. The total accumulated sediment thickness can be measured at each step of the experiment. However, the amount of deposited sediments certainly underestimates the actual sediment flux because (1) we do not consider lateral sediment input by hanging wall strike drainage and (2) the model does not necessarily include the entire hanging wall basin (accommodation space can be missing).

2.2. Tectonic Model

[9] Faulting occurs at regular time intervals and progressively deforms the surface topography. Surface deformation is modeled in three dimensions by a kinematic model based on the planar elastic dislocation solution of *Okada* [1985]. We assume that seismic deformation is accommodated by characteristic earthquakes of magnitude ~7 causing ~2.5 m of slip on a 50 km long fault with 15 km downdip width. The time recurrence of earthquakes is a multiple of the erosional time step and is adjusted to fit the required fault slip rate. The dislocation is applied to every grid node relative to that of the fault trace at the surface in order to keep a constant position of the fault trace in the x, y, and z coordinate system.

[10] The grid is deformed by repeated earthquakes. Without remeshing, the fault scarp would be only defined perpendicularly to its strike by the two nodes located at its top and bottom. In order to maintain a good spatial resolution on the fault scarp and to avoid biases due to uneven grid spacing, regular remeshing was performed by adding a line of nodes on the fault scarp whenever the cumulative horizontal displacement equaled the original grid spacing (here 0.1 km). Flexural isostatic response to erosion and sedimentation is not included in our model, because its effects are negligible given the model area (a few kilometers squared) and compared to the effect of coseismic slip.

2.3. Evolution of Triangular Faceted Spurs

[11] In order to capture the kinematics of faceted spur formation, we first examined the evolution over time of a model run in which faceted spurs were successfully generated (Figure 2 and Animation 1).[1] During the first stages of scarp evolution, numerous channels with narrow parallel catchments flow off the footwall and form notches in the scarp. Next, a competition for drainage area in the footwall causes a number of catchments to increase their surface areas while others disappear [*Ellis et al.*, 1999]. As a consequence, some drainage divides branch together and form new strike-perpendicular spur crests, each terminating at the top of a triangular facet. Facet imbrication appears because the coalescence of two former divides is not complete (Figure 2). After steady state has been reached, the number of catchments is constant (facet imbrication can persist), crest heights and valley depths remain stable, and

---

[1] Animation is available in the HTML.

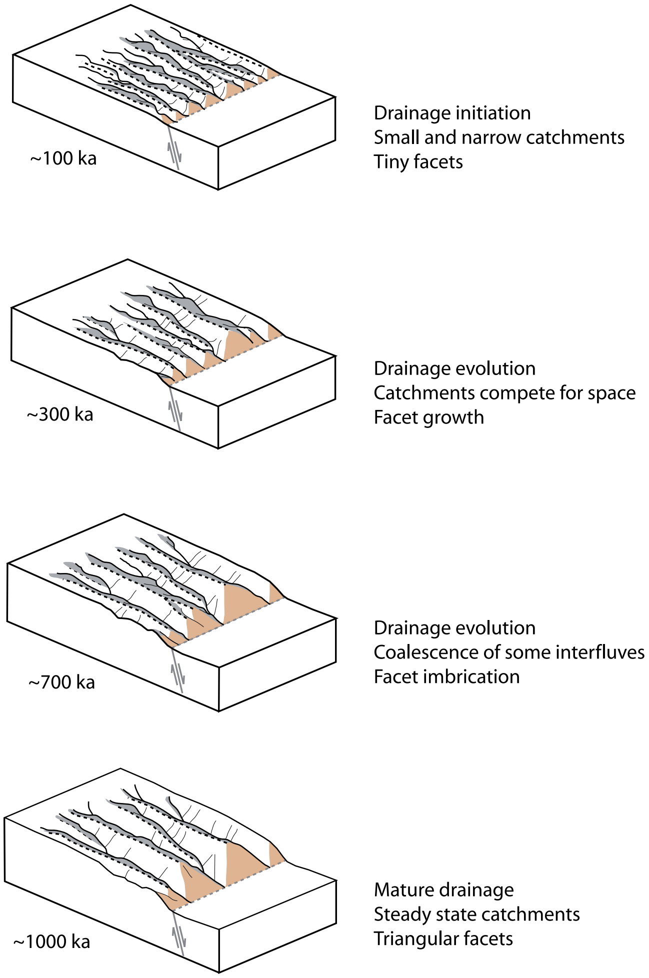

Figure 2. Schematic evolution of a faceted fault scarp based on a successful numerical model (see Animation 1 and text for detailed commentary).

erosion balances out tectonic footwall uplift. The number and shape of triangular facets also remains constant, as they intersect progressively deeper levels of the footwall during exhumation [*Ellis et al.*, 1999]. The time necessary to reach steady state varied between 0.7 and 1 Ma.

3. Results of Parameter Sensitivity Tests

3.1. Climatic Parameters

[12] We first tested the influence of erosion parameters on the development of faceted spurs by successively changing the diffusion coefficient K_D, the effective precipitation rate, v_r, and the characteristic length scale L_f (Figure 3). The transport coefficient K_f equals 0.01. For this set of experiments, the fault is assumed to have a dip angle of 60°, a slip rate of 0.5 mm/a, and the model is run for 1.5 Ma. The initial topography is a gentle (1°) slope in the same direction as the fault dip, with a random white noise of 0.2 m of amplitude. The diffusion coefficient varies between 0.01 and 0.2 m^2/a, the precipitation rate varies from 0.5 to 5 m/a and L_f ranges between 25 and 100 km (Figures 2 and 3). All parameters are constant over the whole grid. These values are similar to those tested in previous studies with the same model formulation [see, e.g., *Kooi and Beaumont*, 1994, 1996; *Densmore et al.*, 1998; *Ellis et al.*, 1999] and correspond to a wide range of scarp shapes. Note, however, that the value of the diffusion coefficient is model-dependent and cannot be compared directly with field measurements. For a given precipitation rate, when diffusion is high and channel bedrock is barely erodible (high L_f and/or low v_r), the scarp is smoothed and not incised. When, instead, the substratum is easily eroded and diffusion is limited, numerous channels develop and the fault scarp becomes deeply incised (Figure 3). Between these two end-member cases, diffusion and incision compete to produce various scarp shapes, including faceted spurs. The latter are found to develop for relatively low diffusion coefficients ($K_D \leq 0.2$ m^2/a) and a moderately high incision rate due either to a high precipitation rate or to high erodibility of the substrate. The sensitivity tests summarized in Figure 3 allow us to determine a characteristic dimensionless diffusion/incision ratio, *f*, for which faceted spurs can develop:

$$f = 10^6 K_D L_f / (v_r S) \tag{5}$$

with *S* being the surface area of the model, implying that $v_r S$ is the total amount of water available for surface runoff (i.e., for mechanical erosion) in the model space ($S \approx 30$ km^2).

[13] Given the initially defined fault dip angle and slip rate and the chosen grid spacing, the *f* ratio suitable for faceted spur development ranges between ~10 and 90 (Figure 3). For *f* values lower than 9, both the scarp and the footwall upland are totally destroyed by river incision, whereas *f* values higher than 700 characterize smoothed scarps with few or no incised channels. For intermediate *f* values ranging between ~100 and ~360, the scarp can either be weakly incised when precipitation and diffusion are low, or display rounded spurs if both precipitation and diffusion are higher. Finally, for *f* values between ~40 and ~100, the scarp can display either triangular or rounded facets depending on whether the diffusion is low or high, respectively. The transition from one morphology to another is progressive and spans a range of *f* values.

3.2. Tectonic Parameters

[14] The influence of tectonic parameters (fault dip angle and slip rate) on the shape of triangular facets was also tested. The fault dip angle was changed from 30 to 75° and the total fault slip rate from 0.25 to 1.5 mm/a, all such changes producing different throw rates as a function of dip angle. Three different erosion parameter sets were tested corresponding to *f* ratio values of 18, 36, and 72 (K_D = 0.05 m^2/a, v_r = 1 m/a, and L_f = 10 km; K_D = 0.05 m^2/a, v_r = 1 m/a, and L_f = 20 km; K_D = 0.1 m^2/a, v_r = 1 m/a, and L_f = 20 km, respectively). Mean facet height was measured as the difference in altitude between the fault trace and the crest of the exhumed fault wall, and mean facet slope was defined perpendicularly to the fault between these two points. Error bars correspond to the standard deviation between the different values.

[15] Results are plotted as a function of throw rate and initial fault dip angle, for each of the three different *f* ratios (Figure 4). The upper graphs on Figure 4 (facet slope) evidence a strong dependence of facet slope on the throw rate for throw rates lower than 0.7 mm/a. In this part of the

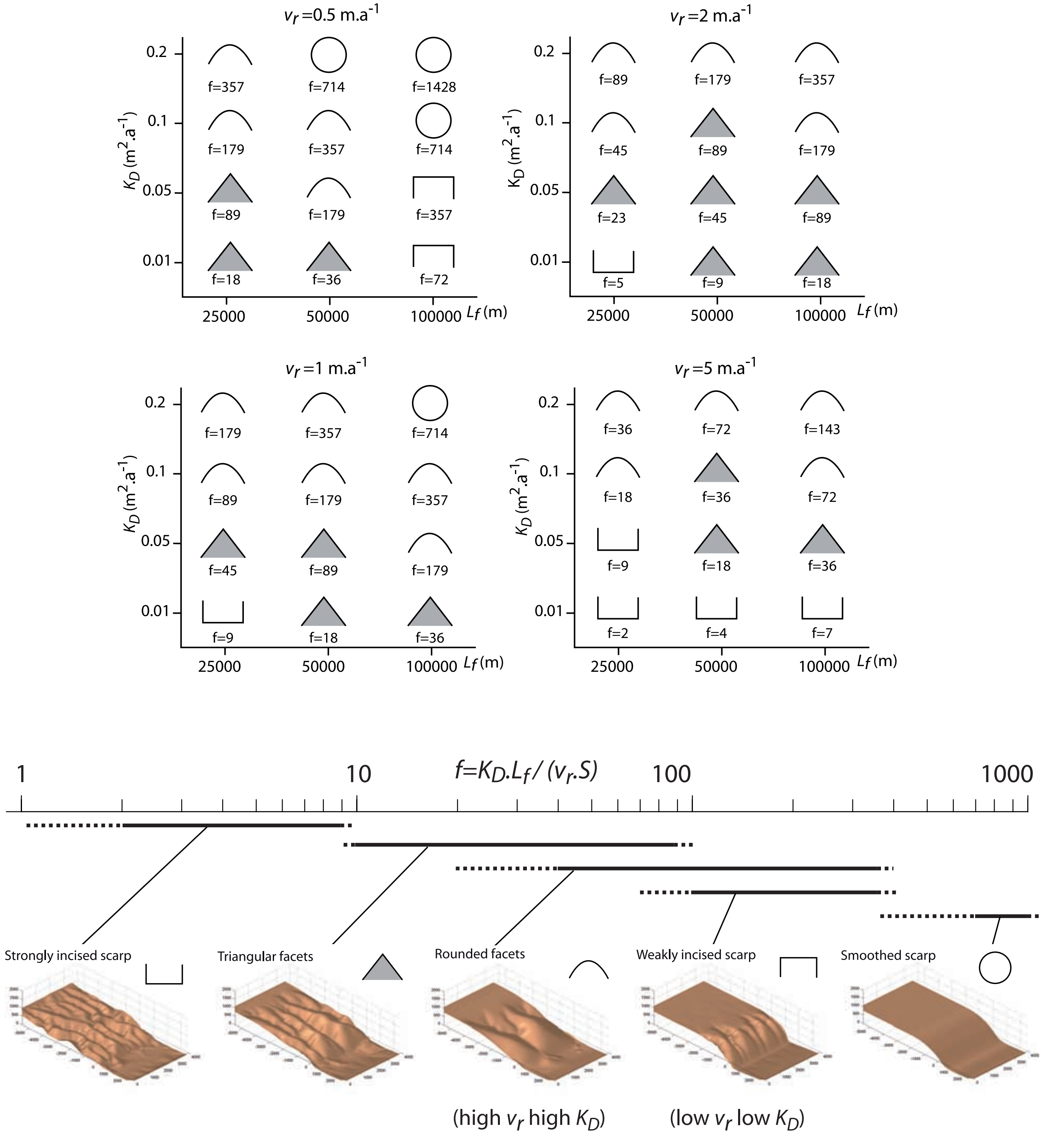

Figure 3. (top and middle) Testing the sensitivity of fault scarp morphology sensitivity to climate-related parameters K_D, v_r, and L_f. These tests demonstrate that faceted spurs develop for an *f* ratio ranging between 10 and 90. (bottom) The geometric symbols depict typical scarp morphologies as a function of *f*.

curve, a higher rate of exhumation produces a steeper slope, and the relationship is linear. Surprisingly, for greater throw rates (and/or for slope angles greater than 25°) the facet slope increases much more slowly. A possible explanation for this behavior lies in the high sensitivity of diffusion to slope curvature: when fault slip is low, erosion is given enough time to smooth the scarp before a new one is created, and few breaks in slope are generated. Conversely, when fault throw rate is high, rapid exhumation of new parts of the fault plane creates large local slope changes that boost erosional processes. As a result, mean scarp slope decreases. Note that this behavior is identical whatever the *f* ratio (18, 36, and 72). Equally surprisingly, mean facet slope does not seem to be primarily controlled by fault dip angle: for given erosion parameters, fresh scarps will be more rapidly eroded when the normal faults dip more steeply than at shallower dip angles, resulting in a similar facet slope whatever the fault dip angle. Finally, facet height appears to

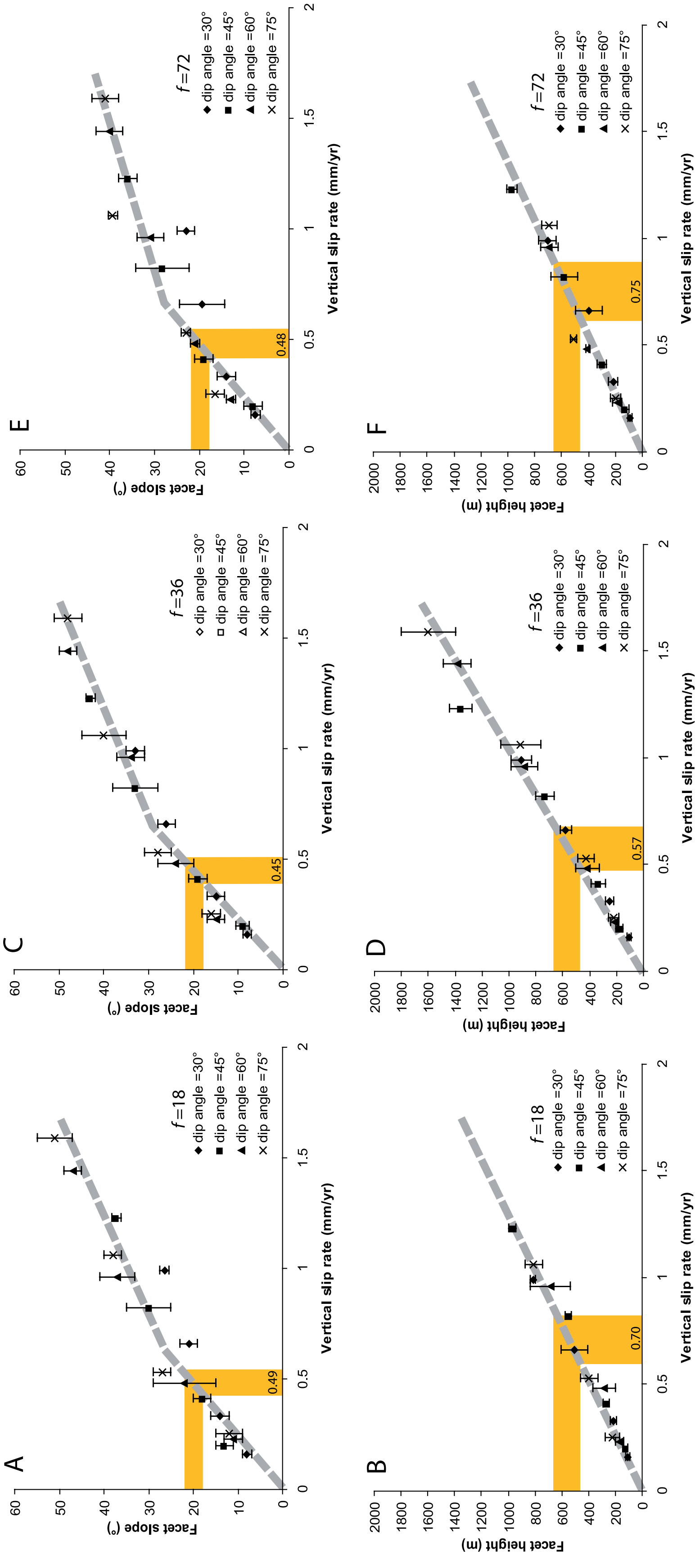
A
B
C
D
E
F
Facet slope (°)
Facet height (m)
Vertical slip rate (mm/yr)
f =18
f =36
f =72
dip angle =30°
dip angle =45°
dip angle =60°
dip angle =75°
0.49
0.70
0.45
0.57
0.48
0.75
0 10 20 30 40 50 60
0 200 400 600 800 1000 1200 1400 1600 1800 2000
0 0.5 1 1.5 2

Figure 4

be a linear function of throw rate irrespective of the fault dip angle, the latter being taken into account in the computation of the throw rate (Figures 4b, 4d, and 4f). It is worth noting that the facet height value does not depend on the duration of the experiment because the facet shape reaches a steady state after a relatively short growth stage (~0.7 to 1 Ma).

[16] The three different erosion parameter sets yield very comparable results in terms of facet slopes and heights, especially for throw rates lower than 1 mm/a (Figure 4). As explained above, this is likely to reflect a predominant role of tectonic processes on facet shape; climatic conditions being subsidiary. For higher throw rates, the values are more scattered and reflect an increasing importance of climatic parameters, especially with respect to facet heights: both high and low *f* ratios (72 and 18, respectively) predict smaller facets compared to an *f* ratio of 36. This suggests that, when erosion is dominated either by diffusion (larger *f* ratio) or incision (lower *f* ratio), the dominant process is so intensely boosted by the tectonic signal that it dampens the influence of the high throw rate on facet height more efficiently than when diffusion and incision balance each other out (intermediate *f* ratios).

[17] In summary, this test shows that, in addition to erosion parameters, the fault throw rate is the main tectonic control on faceted spur shape, here defined by height and fault-perpendicular topographic slope. Fault dip angle does not seem to exert such a strong influence on either facet height or facet mean slope.

4. Application: The Wasatch Fault

4.1. Fault Geometry and Slip Rate

[18] The Wasatch Fault is the longest active normal fault in the United States, and is located at the junction between the Colorado plateau and the Basin and Range system, in Utah (Figures 5 and 6). It is delineated by triangular facets and is made up of several ~50 km long segments [e.g., *Machette et al.*, 1991; *Armstrong et al.*, 2004]. The tectonic characteristics of the Wasatch Fault (Table 1) are well constrained by a large number of studies that have defined its dip, long- or short-term slip rates, earthquake recurrence intervals, and locking depth [see, e.g., *Machette et al.*, 1991; *McCalpin and Nishenko*, 1996; *De Polo and Anderson*, 2000; *Mattson and Bruhn*, 2001; *Malservisi et al.*, 2003; *Armstrong et al.*, 2004]. In this study, we try to assess the average long-term erosion parameters likely to have prevailed during the growth of the Wasatch Fault scarp. We focus on the central portion of the Weber segment of the Wasatch Fault, close to the Great Salt Lake, because (1) its tectonic parameters are well constrained, (2) both its surface trace and the drainage divide are linear, largely parallel to one another (Figure 6), and thus closely match our model geometry, (3) its lithology is homogeneous (quartz monzonite gneiss corresponding to the Precambrian Farmington Canyon complex [*Bryant*, 1988]; see Figure 5), (4) the impact of Pleistocene cirque glaciation on the scarp face is negligible (Figure 6), and (5) the geometry of the drainage network is simple with a suite of short (~5 km), strike-perpendicular perennial streams (Figure 6). Furthermore, the catchments exhibit convex hypsometric curves (not illustrated) with hypsometric integrals (0.4–0.6) typical of young catchments. This configuration suggests that most of the drainage system is contemporaneous with fault development. We also avoided areas with conspicuous landsliding in order to maintain field parameters similar to basic model parameterizations. For that reason, the study area is situated to the north of the Farmington lobe of Quaternary landslide deposits indicated on the 1:100,000 geologic map of the Central Wasatch Front [*Davis*, 1983; *Bryant*, 1988]. Sporadic interlayers of debris flow deposits within the mountain front alluvial fans are reported on the quadrangle geologic maps and suggest intermittently more turbid flow conditions during the Pleistocene and Holocene, but fluvial incision has remained the dominant process.

[19] From low-temperature thermochronology data, *Armstrong et al.* [2004] inferred an age of 3.9–6.4 Ma for the exhumation of the Weber fault segment scarp, and a mean vertical exhumation rate ranging between 0.2 and 0.3 mm/a. The analysis of active facet heights led *De Polo and Anderson* [2000] to infer a mean throw rate of ~0.8 mm/a on the Weber fault segment. Depending on the assumed fault dip (45 or 60° for instance), these values correspond to horizontal slip rates of ~0.4 to ~0.8 mm/a. A comprehensive study of the morphology of faceted spurs has also been carried out by *Zuchiewicz and McCalpin* [2000]. On the Weber segment, these authors measured mean facet heights of 570 ± 100 m, and a mean slope of 20 ± 2°. From the graphics shown on Figure 4, this would correspond to throw rates of 0.6 ± 0.15 mm/a. These values are only indicative as the erosion parameters chosen for the sensitivity tests shown on Figure 4 might not correspond to the Wasatch Fault climatic setting. However, the inferred slip rate is quite consistent with, though slightly lower than, the one found by *De Polo and Anderson* [2000]. The geologic cross section of the Wasatch front in the Weber segment shows a total throw of ~4000 m (Figure 5 after *Hintze* [1974] (modified by G. C. Willis, 2005) and *Yonkee and Lowe* [2004]). Considering the age of exhumation given by *Armstrong et al.* [2004], this yields a throw rate of 0.6 to 1 mm/a.

[20] Numerical models of scarp degradation led *Mattson and Bruhn* [2001] to propose a short-term (10 to 100 ka) total slip rate ranging between 1 and 2 mm/a for the Weber segment (i.e., 0.7 to 1.4 mm/a of horizontal extension and 0.7 to 1.7 mm/a of uplift with the previously assumed fault dip angles). *Nelson and Personius* [1993] described the geometry of recent scarps on the Weber segment in great detail. From their study, the mean total fault slip rate on this

Figure 4. Effect of tectonic parameters (fault throw rate and dip angle) on (a, c, and e) the mean slope and (b, d, and f) height of faceted spurs, for three different erosion conditions (*f* = 18, 36, and 72, respectively, from left to right). Dashed line depicts inferred relationship between tectonic parameters and facet shape. For extreme values of throw rates and fault dip angles, some models succumbed to numerical instabilities and outputs are not illustrated. Orange rectangles represent mean facet slope (Figures 4a, 4c, and 4e) and height (Figures 4b, 4d, and 4f) values for the Wasatch fault according to *Zuchiewicz and McCalpin* [2000] and also mention the corresponding throw rate.

segment is about 1 ± 0.5 mm/a, and the earthquake recurrence interval is about 1200 ± 900 years. This value is roughly similar to the one found by *McCalpin and Nishenko* [1996] based on fault trench analyses (1782 ± 102 years). Characteristic earthquakes are assumed to have a mean magnitude of ~7. Finally, *Malservisi et al.* [2003] modeled the displacements measured by GPS data across the Wasatch Fault by a 45° dipping normal fault in a 10 km thick elastic layer lying above a viscoelastic half-space. Their model yielded instantaneous horizontal extension rates as high as 3.0 to 4.5 mm/a, which is much higher than long-term slip rates obtained by the other methods.

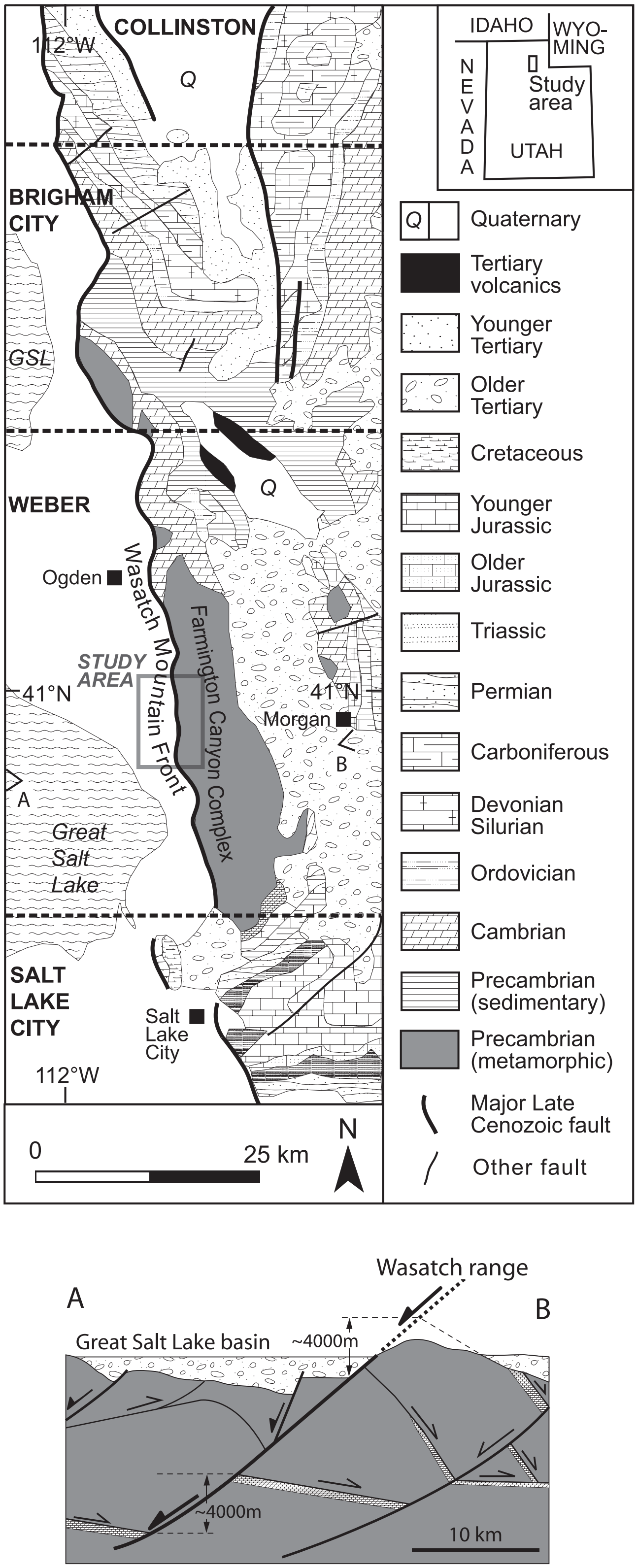

Figure 5. (top) Location map and geologic setting of study area in the Wasatch Mountains, Utah [after *Hintze*, 1974]. The chosen model test area (Weber segment, see also Figure 6) corresponds to the most homogeneous lithological continuum of the Wasatch (Precambrian gneiss), and one of the straightest segments of the mountain front. Tectonic subdivison of the Wasatch Fault into segments (delimited by horizontal dashed lines) after *Machette et al.* [1991]. (bottom) Cross section AB (between points A and B in Figure 5 (top)) and estimates of the total throw (interpreted after *Yonkee and Lowe* [2004]).

[21] In summary, with the exception of GPS-based models, which predict a much higher value, previous studies of the Weber fault segment estimate a mean long-term total slip rate of about 0.75 ± 0.45 mm/a. Assuming a mean segment length of 50 km, a downdip width of about 15 km and a mean coseismic slip of 1 m, this slip rate corresponds to a characteristic earthquake of magnitude ~7 every 500 to 1500 years, which is in good agreement with observed recurrence intervals. On the basis of those studies, the throw rate is thus estimated to lie within the 0.3–1 mm/a bracket depending on the assumed fault dip angle (45 or 60°), which is only a crude estimate. Our model allows us to narrow the range of acceptable throw rates to 0.45–0.75 mm/a (Figure 4). Clearly, such estimates do not take into account possible temporal variations of the slip and throw rates, which are beyond the resolution of our model.

4.2. Inversion of Climatic Parameters

[22] Here we test our model on the Weber scarp in order to retrieve the mean values of climatic parameters (i.e., K_D, L_f, and v_r) that would have prevailed during its development. On the basis of the previously presented tectonic constraints, we assume the following fault characteristics: 50 km length, 10 km locking depth, 45° dip, vertical slip rate of 0.6 mm/a (according to our estimates, see Figure 4), fault age of 5 Ma. A common difficulty in surface process modeling is to define an objective ranking of the output models (see *Dietrich et al.* [2003] on visual realism and the choice of morphologic properties when testing SPMs). In this study, we chose to implement a more objective evaluation of the quality of fit by computing a root-mean-square (RMS) residual, defined as the mean error between the reference and computed 2.5-D topography:

$$\mathrm{RMS} = \sqrt{\frac{\sum_{1}^{N}\left(h_{\mathrm{obs}(x,y)} - h_{\mathrm{comp}(x,y)}\right)^2}{N}} \tag{6}$$

Here, the reference topography was defined by the 90 m Shuttle Radar Topography Mission digital elevation grid, resampled to a 100 × 100 m pixel size in order to match the model grid dimensions. In order to avoid unwanted noise from the upstream drainage catchments interfering with

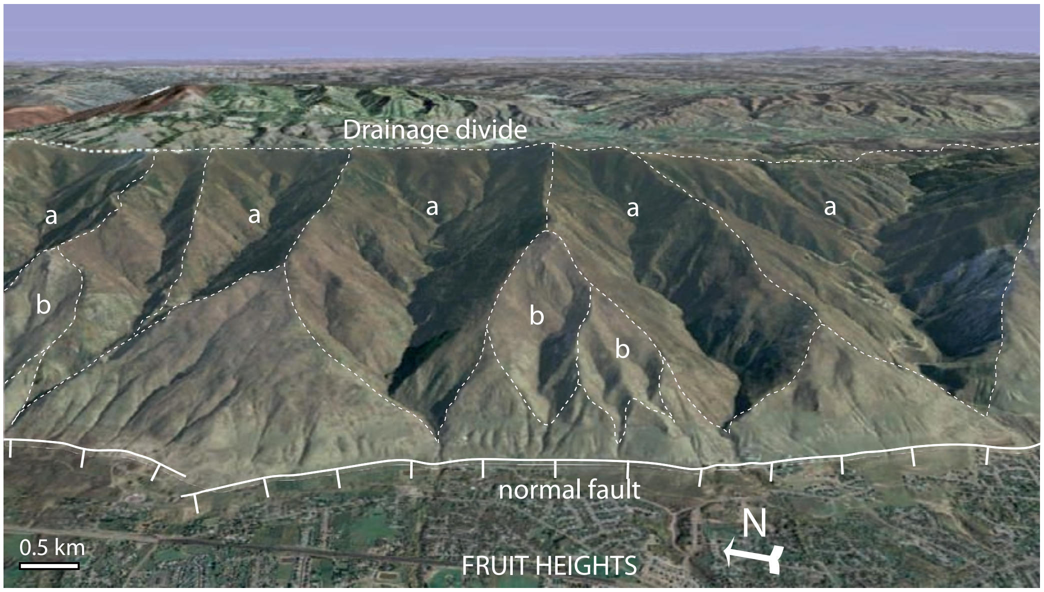

Figure 6. View of the study area (Weber segment) generated from ortho images draped over a USGS digital elevation model. Ortho image ground sample distance (GSD) of 1 m (source is National Agricultural Imagery Program, 2006). NAIP quarter quadrangles are rectified to the UTM coordinate system NAD83. The USGS digital elevation model (GSD = 10 m) is a 1-degree DEM (3 by 3 arc sec data spacing). The 1-degree DEM consists of a regular array of elevations referenced horizontally on the geographic (latitude/longitude) coordinate system of the WGS-84 and converted to the UTM coordinate system NAD83. Additional source is the Utah GIS Portal. The main drainage divide trending parallel to the fault strike is indicated as a, main facet-bounding catchments; and b, older fault-perpendicular catchments (see Figure 2 and Animation 1).

error computations relevant to scarp morphology, the RMS calculation was restricted to a narrow, strike-parallel swath of the topographic grid covering the scarp and its triangular facets. Without any other constraints, the modeled river network depends on the random noise superimposed on the initial topography. Any 2.5-D error will therefore be affected by slight mismatches in river channel locations more than by the morphology of the fault scarp. To overcome this problem, initial model conditions involved grooving the model grid topography (a 1° slope in the same direction as the fault dip) to depths of just a few meters at locations dictated by observed stream spacing in the digital elevation model of the Weber segment. Such a procedure forces the rivers to flow in channels positioned in those predefined locations, with the result that model outputs generate models that are objectively realistic in terms of stream spacing with respect to the Weber segment topography. Any RMS error is thus unlikely to be contributed by channel offsets between the model and the reference topographies. These initial surface conditions thus defined only control the resulting facet width. We next performed a Monte Carlo inversion consisting of 190 runs, sampling random values of K_D, L_f and v_r between 0.05 and 0.15 m^2/a, 15 and 35 km and 1 and 3 m/a, respectively.

[23] RMS results for the 190 tests were interpolated to generate a continuous RMS map for different values of K_D and v_r (Figure 7), with $K_f = 0.01$. The map shows a clear RMS minimum for $0.11 \leq K_D \leq 0.13$ m^2/a and $v_r = 1.1$ m/a. This set of values represents the average erosion conditions for the 5 Ma period considered here. No clear minimum, however, appeared for L_f. Indeed, since L_f predominantly controls the river length scale, error maps computed close to the river mouth will not be sensitive to variations in L_f variations. Other synthetic tests and a visual estimation of the topographic resemblance between the model and reference topographies tend to indicate that low values of L_f (around 15 km) might provide a better fit to the data. The mean annual effective rainfall (v_r) value of 1.2 m/a is also realistic for the Weber segment, where 1961–1990 annual rainfall totals on the mountain front are given as 1–1.5 m (http://www.nationalatlas.gov/printable/images/pdf/precip/pageprecip_ut3.pdf). The presence of large lakes during the colder Pleistocene epochs suggests wetter climates, and it has been argued that the lakes were formed both because of lower evaporation rates relating to lower mean temperatures [*Hostetler et al.*, 1994; *Kaufman*, 2003] and because of greater precipitation rates [*Benson and Thompson*, 1987; *Oviatt*, 1997]. Humid climates do not systematically result in large runoff rates (i.e., large v_r). Humid climates may also promote denser vegetation, deeper weathering, and the rounding of hillslope profiles as a consequence of enhanced slope diffusion [e.g., *Kooi and Beaumont*, 1994]. Because the climatic parameter, v_r, is a proxy for bedrock erosional response to climatic conditions rather than a direct expression of specific weather systems and past atmospheric conditions, the relatively high diffusion coefficient obtained for the Wasatch range might thus

Table 1. Tectonic Characteristics of the Wasatch Fault Zone From Previous Studies[a]

TSR (mm/a)	HSR (mm/a)	VSR (mm/a)	α (deg)	H (m)	S (deg)	ER (years)	References
0.5–1.5	*0.2–1.1*	*0.3–1.3*	*45–60*			**1200 ± 900**	*Nelson and Personius* [1993]
			45–60			**1787 ± 102**	*McCalpin and Nishenko* [1996]
0.9–1.1	*0.4–0.8*	**0.8**	*45–60*				*De Polo and Anderson* [2000]
0.7–1.1	*0.4–0.8*	*0.45–0.75*	*45–60*	**470–670**	**18–22**		*Zuchiewicz and McCalpin* [2000]
1–2	*0.5–1.4*	*0.7–1.7*	*45–60*				*Mattson and Bruhn* [2001]
4.2–6.4	**3–4.5**	*3–4.5*	**45**				*Malservisi et al.* [2003]
0.2–0.4	*0.1–0.3*	**0.2–0.3**	*45–60*				*Armstrong et al.* [2004]

[a] Age is 3.9–6.4 Ma. TSR, HSR, and VSR refer to total, horizontal, and vertical slip rates, respectively; α is the fault dip angle, H is the facet height, S is the facet slope, ER is the earthquake recurrence interval. Numbers in bold correspond to published values, and numbers in italics are those that could be deduced from the latter.

reflect the effect of wetter intervals that prevailed during enhanced glacial conditions.

[24] Overall, the optimal RMS parameterization corresponds to an f value band of 46 to 54, which falls well within the range required for the development of triangular facets as proposed in Figures 2 and 3. Figure 4 tends to indicate that the facet height/throw rate line has a steeper slope for high f values (36 or 72) than for low ones (18). As the inversion is very sensitive to facet height (which will strongly affect the RMS value) it is likely that an error in the fault throw rate (whatever its sense) will bias the result toward larger f values, i.e., larger diffusion coefficient of characteristic length scale, or lower precipitation rates. The resulting topography (Figure 8) depicts ~2 km wide, 560 m high triangular facets with an average slope of 23°, hence very similar to those observed on the Weber segment scarp [*Zuchiewicz and McCalpin*, 2000]. The facet-perpendicular topographic profile is also well reproduced (Figure 8c). The total sediment thickness accumulated during the 5 Ma time span (about 400 m) underestimates the actual ~2000 m of sediment present in the Great Salt Lake basin at the foot of the escarpment [*Yonkee and Lowe*, 2004]. However, our results cannot be compared with the total Cenozoic sedimentary sequence of the Wasatch front basin because the model accounts neither for the real basin configuration (geometry, sediments sources, subsidence and flexure and accommodation space), nor for the occurrence of synsedimentary faults within the basin.

5. Discussion

[25] We developed a simple coupled SPM and tectonic model which allows us to determine the conditions of growth of faceted spurs at normal fault scarps. Our sensitivity tests indicate that a fault scarp bears faceted spurs only when diffusion and incision processes balance out (Figure 3). In other conditions, the scarp is either smoothed or dissected.

[26] Other tests performed allow defining a characteristic f diffusion/incision ratio that determines the climatic conditions suitable for the development of faceted spurs. For a model surface of ~30 km^2, suitable conditions are met when f ranges between 10 and ~90. Figure 3 shows that this theoretical range of values covers a wide spectrum of the variables K_D, L_f, and v_r. For example, we find that $f = 36$ is valid for settings where v_r values can be anything between 0.5 (arid) and 5 m/a (hyperhumid) while letting K_D and L_f vary accordingly. Similar conclusions can be drawn when $f = 72$ or $f = 89$. This suggests that similar landforms are produced when rainfall varies by 1 order of magnitude, and that the formation of faceted scarps is therefore not strongly limited to particular climatic conditions. This conclusion is supported by the fact that faceted spurs and scarps occur in a wide range of climatic settings around the world.

[27] Tests performed using different tectonic parameters (fault dip angle and slip rate) and three different f ratios have also indicated that the fault dip angle does not significantly affect mean facet height or slope. Both attributes are instead predominantly controlled by the throw rate, a finding that is at odds with the conclusions of *Ellis et al.* [1999]. However, f ratios corresponding to either dissection-dominated or diffusion-dominated erosion seem to dampen the influence of the fault throw rate on facet height. Fault dip angle obviously has a strong influence on facet *height*, as it controls the amount of vertical uplift for a given extension rate. However, its long-term influence on facet *slope* is minor because the facet almost always retreats back from the fault plane and its gradient declines, except at the scarp foot where rejuvenation by the last few earthquakes has occurred. The models thus indicate that steep fault planes will initially produce steep scarps in which slope declines

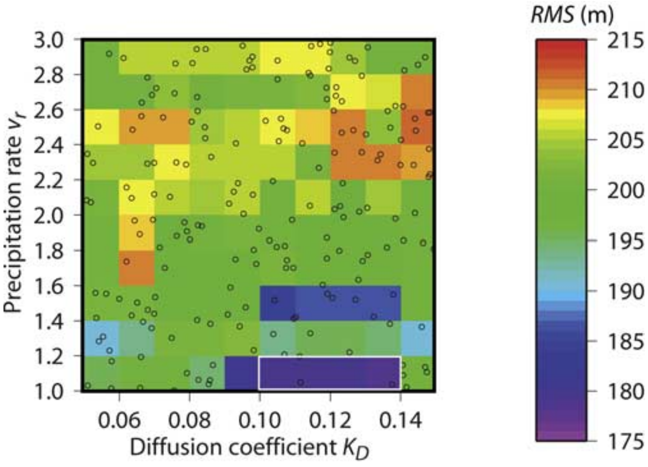

Figure 7. Results of a Monte Carlo inversion for the effective precipitation rate (vertical axis) and diffusion coefficient (horizontal axis) on the Weber segment of the Wasatch Fault. Color scale refers to the root-mean-square residual (RMS in meters) between the observed and modeled topography. Open circles indicate the parameters tested. A visible minimum (blue color, circled) is found for low effective precipitation rates (~1.1 m/a) and relatively high (0.12 m^2/a) diffusion coefficients (best fitting models are delineated by the white rectangle).

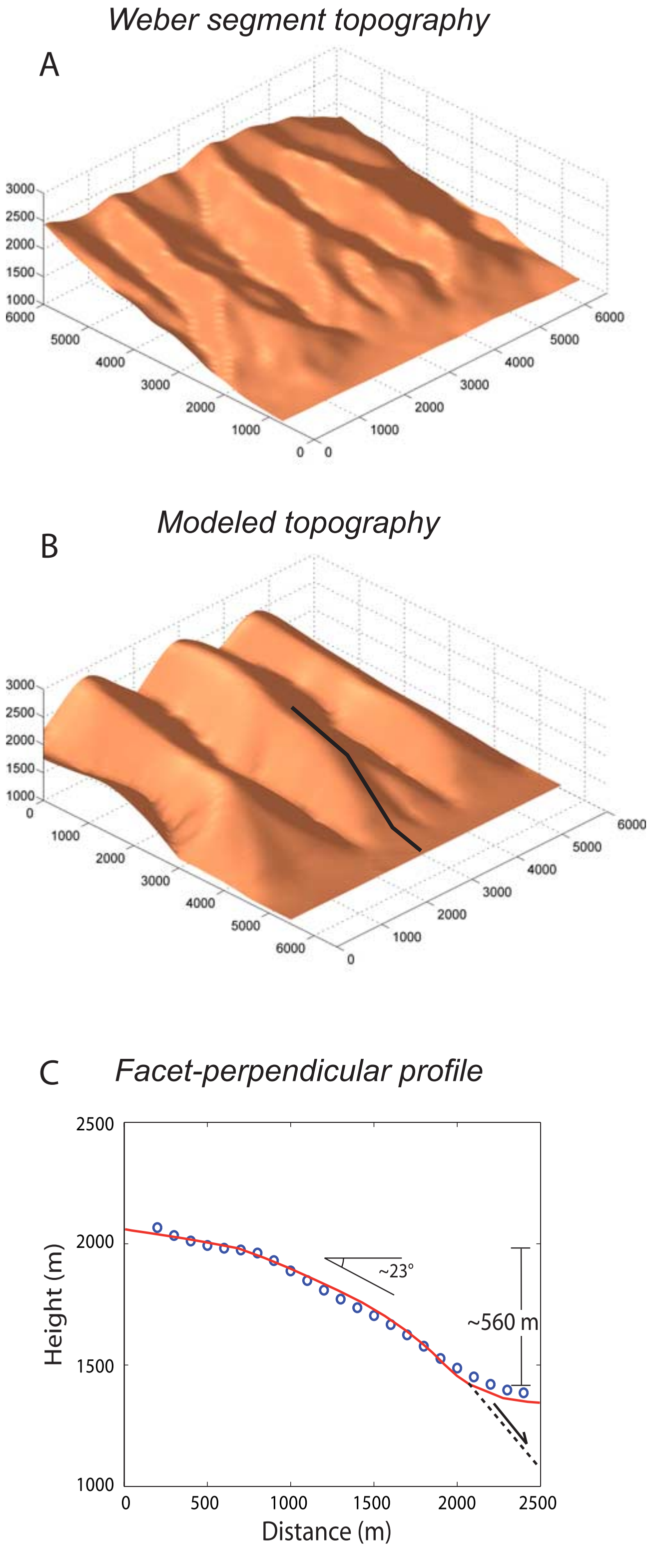

Figure 8. (a) Observed and (b) modeled 2.5-D topography for the best fitting parameters determined from the Monte Carlo inversion (see Figure 7). (c) Observed and modeled facet-perpendicular profiles (solid line in Figure 8b indicates profile location).

rapidly because of erosion, whereas low-dipping fault planes will produce more gently sloped scarps where erosion is accordingly less active, resulting in facet slope angles that remain similar to the fault dip.

[28] It follows that with even a rough approximation of the average climatic parameters (rainfall and diffusion coefficient), the measurement of facet slopes and heights can help estimate an unknown throw rate [*Ganas et al.*, 2005]. Conversely, when average fault dip angle and slip rates are known, it is possible to recover the approximate rainfall parameters that prevailed during scarp evolution by inversion of the 2.5-D scarp topography. A Monte Carlo inversion on the Weber segment of the Wasatch Fault shows that the 5 Ma long development of this fault scarp has been dominated by a low effective precipitation rate ($\sim$1 m/a) and a moderate diffusion coefficient (0.13 m^2/a), its long-term throw rate of $\sim$0.6 mm/a being determined from average facet height prior to the inversion. The 2.5-D scarp shape and the fault-perpendicular profile are successfully retrieved, though the amount of sediments deposited at the foot of the scarp cannot be directly compared with the late Cenozoic sediment thickness inferred from geologic cross section [*Yonkee and Lowe*, 2004].

[29] The limitations of our model arise in part from the use of numerical parameters that are not easy to measure in the field: the f ratio, for example, depends upon parameters derived from incision and diffusion laws, which cannot be measured directly. The f ratio is also grid-dependent because the amount of incision/deposition and the diffusion rate depend on the grid spacing. This, however, can be readily tested by varying grid cell size in model grids and by using reference topographies corresponding to different DEM resolutions. The assumption that flexural isostatic response of the lithosphere is negligible remains valid for a small area close to the fault, such as that studied here for the Weber segment, but would not hold true on the scale of a whole mountain range and its adjacent basin, hundreds of kilometers squared. Isostasy can readily be included in models when appropriate. Moreover, the inverted diffusion coefficient and effective precipitation rate only represent a long-term (Pliocene to Pleistocene) average of the erosional conditions that prevailed during the development of this segment of the Wasatch Fault. Depending on the resolution of available data, a higher resolution model could be used to obtain greater precision on facet evolution, for example as a function of glacial and interglacial episodes, and incorporate temporal variations in slip rate responsible for transient landscape signatures.

[30] Our study has focused on steady state topographic systems, i.e., where tectonics and erosion are in equilibrium. Transient landscapes, however, also exist in active footwall uplands, and useful tectonic information can be retrieved from drainage patterns and river long profiles to evidence this [e.g., *Whittaker et al.*, 2008]. Nevertheless, the steady state assumption allows us to constrain the mean fault throw rate from facet heights and slopes. In the case of a transient topography, this would not be possible. Our model also does not include any considerations on the history of fault growth, interaction and linkage. In the Wasatch worked example, data on these aspects do not exist. However, as argued by *Ellis et al.* [1999], the steady state configuration that we are concerned with is only weakly dependent upon

the initial stages of fault evolution. As a result, treating the kinematics of fault initiation and linkage as a black box is not detrimental to the value of the model as an experimental tool in tectonic geomorphology.

6. Conclusion

[31] We have presented a numerical surface process model and shown how it can be used as a tool for constraining the climatic and tectonic parameters that control the development of faceted spurs at normal fault scarps. Sensitivity tests allowed us to define a dimensionless ratio of erosion, *f*, for which triangular faceted spurs, as opposed to any other alternative range front morphology, can develop. The study evidences a strong dependence of facet slope angle on throw rate for throw rates between 0.4 and 0.7 mm/a. Facet height also appears to be linearly dependent upon the fault throw rate. Model performance was tested on the Wasatch Fault, using topographic, geologic and seismologic data for calibration purposes. Overall, results demonstrate the ability of our model to estimate normal fault throw rates from the height and slope of triangular facets, and to retrieve the average long-term diffusion and incision parameters that prevailed during scarp evolution. Despite the limitations examined in the Discussion, our model suggests that active geomorphic markers such as triangular faceted spurs can help to determine the long-term throw rate of active faults at mountain fronts. More detailed information on the fault slip rate and slip direction could be obtained using a model involving mixed normal and strike-slip motions.

[32] **Acknowledgments.** The authors are grateful to Richard Arculus (Editor), Paul Bishop, Alex Whittaker, and one anonymous reviewer for their constructive remarks which helped us to improve the final version of this manuscript.

References

Allen, P. A., and A. L. Densmore (2000), Sediment flux from an uplifting fault block, *Basin Res.*, *12*, 367–380, doi:10.1046/j.1365-2117.2000.00135.x.

Anderson, R. S. (1994), Evolution of the Santa Cruz Mountains, California, through tectonic growth and geomorphic decay, *J. Geophys. Res.*, *99*, 20,161–20,174, doi:10.1029/94JB00713.

Armijo, R., H. Lyon-Caen, and D. Papanastassiou (1991), A possible normal-fault rupture of the 464 BC Sparta earthquake, *Nature*, *351*, 137–139, doi:10.1038/351137a0.

Armstrong, P. A., A. R. Taylor, and T. A. Ehlers (2004), Is the Wasatch fault footwall (Utah, United States) segmented over million-year time scales?, *Geology*, *32*, 385–388, doi:10.1130/G20421.1.

Attal, M., G. E. Tucker, A. C. Whittaker, P. A. Cowie, and G. P. Roberts (2008), Modeling fluvial incision and transient landscape evolution: Influence of dynamic channel adjustment, *J. Geophys. Res.*, *113*, F03013, doi:10.1029/2007JF000893.

Beaumont, C., P. Fullsack, and J. Hamilton (1992), Erosional controls of active compressional orogens, in *Thrust Tectonics*, edited by K. R. McClay, pp. 1–18, Chapman and Hall, New York.

Benedetti, L., P. Tapponnier, G. C. P. King, and L. Piccardi (1998), Surface rupture of the 1857 southern Italian earthquake?, *Terra Nova*, *10*, 206–210, doi:10.1046/j.1365-3121.1998.00189.x.

Benson, L., and R. S. Thompson (1987), The physical record of lakes in the Great Basin, in *The Geology of North America, vol. K3, North American and Adjacent Oceans During the Last Deglaciation*, edited by W. F. Ruddiman and H. E. Wright Jr., pp. 241–260, Geol. Soc. of Am., Boulder, Colo.

Birot, P. (1958), *Morphologie structurale*, vol. 1, 177 pp., Presses Univ. de Fr., Paris.

Braun, J. (2006), Recent advances and current problems in modelling surface processes and their interaction with crustal deformation, in *Analogue and Numerical Modelling of Crustal-Scale Processes*, edited by S. J. H. Buiter and G. Schreurs, *Geol. Soc. Spec. Publ.*, vol. 253, pp. 307–325.

Braun, J., and M. Sambridge (1997), Modelling landscape evolution on geologic time scales: A new method based on irregular spatial discretization, *Basin Res.*, *9*, 27–52, doi:10.1046/j.1365-2117.1997.00030.x.

Bryant, B. (1988), Geology of the Farmington Canyon complex, Wasatch Mountains, Utah, geological map, scale , 1:50,000, *U.S. Geol. Surv. Prof. Pap.*, *1476*, 54 pp.

Codilean, A. T., P. Bishop, and T. B. Hoey (2006), Surface process models and the links between tectonics and topography, *Prog. Phys. Geogr.*, *30*, 307–333, doi:10.1191/0309133306pp480ra.

Cotton, C. A. (1950), Tectonic scarps and fault valleys, *Geol. Soc. Am. Bull.*, *61*, 717–758, doi:10.1130/0016-7606(1950)61[717:TSAFV]2.0.CO;2.

Coulthard, T. (2001), Landscape evolution models: A software review, *Hydrol. Process.*, *15*, 165–173, doi:10.1002/hyp.426.

Cowie, P. A., M. Attal, G. E. Tucker, A. C. Whittaker, M. Naylor, A. Ganas, and G. P. Roberts (2006), Investigating the surface process response to fault interaction and linkage using a numerical modelling approach, *Basin Res.*, *18*, 231–266.

Davis, F. D. (1983), Geologic map of the central Wasatch Front, Utah, *Map 44-A*, Utah Geol. and Miner. Surv., Salt Lake City.

Densmore, A. L., M. A. Ellis, and R. S. Anderson (1998), Landsliding and the evolution of normal-fault-bounded mountains, *J. Geophys. Res.*, *103*, 15,203–15,219, doi:10.1029/98JB00510.

Densmore, A. L., N. H. Dawers, S. Gupta, R. Guidon, and T. Goldin (2004), Footwall topographic development during continental extension, *J. Geophys. Res.*, *109*, F03001, doi:10.1029/2003JF000115.

Densmore, A. L., P. A. Allen, and G. Simpson (2007), Development and response of a coupled catchment fan system under changing tectonic and climatic forcing, *J. Geophys. Res.*, *112*, F01002, doi:10.1029/2006JF000474.

De Polo, C. M., and J. G. Anderson (2000), Estimating the slip rates of normal faults in the Great Basin, USA, *Basin Res.*, *12*, 227–240, doi:10.1046/j.1365-2117.2000.00131.x.

Dietrich, W. E., D. G. Bellugi, L. S. Sklar, J. D. Stock, A. M. Heimsath, and J. J. Roering (2003), Geomorphic transport laws for predicting landscape form and dynamics, in *Prediction in Geomorphology*, *Geophys. Monogr. Ser.*, vol. 135, edited by P. R. Wilcock and R. I. Iverson, pp. 103–113, AGU, Washington, D. C.

Ellis, M. A., A. L. Densmore, and R. S. Anderson (1999), Development of mountainous topography in the Basin and Range, USA, *Basin Res.*, *11*, 21–41, doi:10.1046/j.1365-2117.1999.00087.x.

Ganas, A., S. Pavlides, and V. Karastathis (2005), DEM-based morphometry of range-front escarpments in Attica, central Greece, and its relation to fault slip rates, *Geomorphology*, *65*, 301–319, doi:10.1016/j.geomorph.2004.09.006.

Gilchrist, A. R., H. Kooi, and C. Beaumont (1994), The post-Gondwana geomorphic evolution of southwestern Africa: Implications for the controls on landscape development from observations and numerical experiments, *J. Geophys. Res.*, *99*, 12,211–12,228, doi:10.1029/94JB00046.

Goldsworthy, M., and J. Jackson (2000), Active normal fault evolution in Greece revealed by geomorphology and drainage patterns, *J. Geol. Soc.*, *157*, 967–981.

Hamblin, W. K. (1976), Patterns of displacement along the Wasatch Fault, *Geology*, *4*, 619–622, doi:10.1130/0091-7613(1976)4<619:PODATW>2.0.CO;2.

Hintze, L. F. (1974), Geologic map of Utah, scale , 1:2,500,000, Utah Geol. Surv., Salt Lake City.

Hostetler, S. W., F. Giorgi, G. T. Bates, and P. J. Bartlein (1994), Lake–atmosphere feedbacks associated with paleolakes Bonneville and Lahontan, *Science*, *263*, 665–668, doi:10.1126/science.263.5147.665.

Houdry, F. (1994), Mécanismes de l'extension continentale dans le rift Nord-Baïkal, Sibérie: Contraintes des données d'imagerie SPOT, de terrain, de sismologie et de gravimétrie, Ph.D. thesis, 345 pp., Univ. Pierre et Marie Curie, Paris.

Kaufman, D. S. (2003), Amino acid paleothermometry of Quaternary ostracodes from the Bonneville Basin, Utah, *Quat. Sci. Rev.*, *22*, 899–914, doi:10.1016/S0277-3791(03)00006-4.

Kooi, H., and C. Beaumont (1994), Escarpment evolution on high-elevation rifted margins: Insights derived from a surface processes model that combines diffusion, advection and reaction, *J. Geophys. Res.*, *99*, 12,191–12,210, doi:10.1029/94JB00047.

Kooi, H., and C. Beaumont (1996), Large-scale geomorphology: Classical concepts reconciled and integrated with contemporary ideas via surface processes model, *J. Geophys. Res.*, *101*, 3361–3386, doi:10.1029/95JB01861.

Lague, D., A. Crave, and P. Davy (2003), Laboratory experiments simulating the geomorphic response to tectonic uplift, *J. Geophys. Res.*, *108*(B1), 2008, doi:10.1029/2002JB001785.

Machette, M. N., S. F. Personius, A. R. Nelson, D. P. Schwartz, and W. R. Lund (1991), The Wasatch fault zone, Utah–segmentation and history of Holocene earthquakes, *J. Struct. Geol.*, *13*, 137–139, doi:10.1016/0191-8141(91)90062-N.

Malservisi, R., T. H. Dixon, P. C. La Femina, and K. P. Furlong (2003), Holocene slip rate of the Wasatch fault zone, Utah, from geodetic data: Earthquake cycle effects, *Geophys. Res. Lett.*, *30*(13), 1673, doi:10.1029/2003GL017408.

Mattson, A., and R. L. Bruhn (2001), Fault slip rates and initiation age based on diffusion equation modelling: Wasatch fault zone and eastern Great basin, *J. Geophys. Res.*, *106*, 13,739–13,750, doi:10.1029/2001JB900003.

McCalpin, J. P., and S. P. Nishenko (1996), Holocene paleoseismicity, temporal clustering, and probabilities of future large (M > 7) earthquakes on the Wasatch fault zone, Utah, *J. Geophys. Res.*, *101*, 6233–6253, doi:10.1029/95JB02851.

Merritts, D., and M. Ellis (1994), Introduction to special section on tectonics and topography, *J. Geophys. Res.*, *99*, 12,135–12,141, doi:10.1029/94JB00810.

Meyer, B., R. Armijo, and D. Dimitrov (2002), Active faulting in SW Bulgaria: Possible surface rupture of the 1904 Struma earthquake, *Geophys. J. Int.*, *148*, 246–255, doi:10.1046/j.0956-540x.2001.01589.x.

Nelson, A. R., and S. F. Personius (1993), Surficial geologic map of the Weber segment, Wasatch Fault zone, Weber and Davis counties, Utah, *U.S. Geol. Surv. Misc. Invest. Ser., Map I-2199*, 22 pp.

O'Callaghan, J. F., and D. M. Mark (1984), The extraction of drainage networks from digital elevation data, *Comput. Visual Graph. Image Process.*, *28*, 328–344.

Okada, Y. (1985), Surface deformation to shear and tensile faults in a half-space, *Bull. Seismol. Soc. Am.*, *75*, 1135–1154.

Oviatt, C. G. (1997), Lake Bonneville fluctuations and global climate change, *Geology*, *25*, 155–158, doi:10.1130/0091-7613(1997)025<0155:LBFAGC>2.3.CO;2.

San'kov, V., J. Déverchère, Y. Gaudemer, F. Houdry, and A. Filippov (2000), Geometry and rate of faulting in the North Baikal rift, Siberia, *Tectonics*, *19*, 707–722, doi:10.1029/2000TC900012.

Stock, J., and W. E. Dietrich (2003), Valley incision by debris flows: Evidence of a topographic signature, *Water Resour. Res.*, *39*(4), 1089, doi:10.1029/2001WR001057.

Wallace, R. E. (1978), Geometry and rates of change of fault-related fronts, north-central Nevada, *J. Res. U. S. Geol. Surv.*, *6*, 637–650.

Whittaker, A. C., P. A. Cowie, M. Attal, G. E. Tucker, and G. P. Roberts (2007), Bedrock channel adjustment to tectonic forcing: Implications for predicting river incision rates, *Geol. Soc. Am. Bull.*, *35*, 103–106.

Whittaker, A. C., M. Attal, P. A. Cowie, G. E. Tucker, and G. P. Roberts (2008), Decoding temporal and spatial patterns of fault uplift using transient river long profiles, *Geomorphology*, *100*, 506–526, doi:10.1016/j.geomorph.2008.01.018.

Wobus, C., K. X. Whipple, E. Kirby, N. Snyder, J. Johnson, K. Spyropolou, B. Crosby, and D. Sheehan (2006), Tectonics from topography: Procedures, promises and pitfalls, in *Tectonics, Climate and Landscape Evolution*, edited by S. D. Willett et al., *Spec. Pap. Geol. Soc. Am.*, vol. 398, pp. 55–74.

Yonkee, A., and M. Lowe (2004), Geologic map of the Ogden 7.5-minute quadrangle, Weber and Davis counties, Utah, report, 46 pp., Utah Geol. Surv., Salt Lake City.

Zuchiewicz, W. A., and J. P. McCalpin (2000), Geometry of faceted spurs on an active normal fault: Case study of the central Wasatch fault, Utah, U.S.A., *Ann. Soc. Geol. Poloniae*, *70*, 231–249.

N. Gonga-Saholiariliva and Y. Gunnell, Laboratoire de Géographie Physique, UMR 8591, Université Paris VII, CNRS, Boîte 7001, 2 Place Jussieu, F-75251 Paris CEDEX 05, France.

B. Meyer and C. Petit, ISTeP, UMR 7193, UPMC, CNRS, Tour 46-00 E2, Boîte 129, 4 Place Jussieu, F-75252 Paris CEDEX, France. (carole.mariani@upmc.fr)

J. Séguinot, LGIT, Université Joseph Fourier, BP 53, F-38041 Grenoble CEDEX 9, France.